Dissipative Selection of Low-Frequency Modes in a Reduced-Gravity Basin

PAOLA CESSI AND FRANÇOIS PRIMEAU

Scripps Institution of Oceanography, La Jolla, California

(Manuscript received 28 September 1999, in final form 27 March 2000)

ABSTRACT

The spectrum of linear free modes of a reduced-gravity ocean in a closed basin with weak dissipation is examined. The constraint of total mass conservation, which in the quasigeostrophic formulation determines the pressure on the boundary as a function of time, allows the existence of selected large-scale, low-frequency basin modes that are very weakly damped in the presence of dissipation.

These weakly damped modes can be quasi-resonantly excited by time-dependent forcing near the eigenperiods, or during the process of adjustment to Sverdrup balance with a steady wind from arbitrary initial conditions. In both cases the frequency of the oscillations is a multiple of $2\pi/t_0$, where t_0 is the long Rossby wave transit time, which is of the order of decades for midlatitude, large-scale basins. These oscillatory modes are missed when the global mass conservation constraint is overlooked.

1. Introduction

The analysis of historical North Atlantic sea-level data has revealed fluctuations on the decadal timescale of the order of 10–20 cm. These fluctuations penetrate to the base of the thermocline and are forced by low-frequency variability in the wind-stress (Sturges and Hong 1995; Sturges et al. 1998). Thus there are large redistributions of heat in the ocean that are forced by the atmosphere.

Assuming that some mechanism exists for the generation of power at low frequencies in the atmospheric circulation, we show that the linear response of the upper ocean to wind forcing is quasi-resonant at special periods, determined by the reciprocal multiples of the transit time of long baroclinic Rossby waves in the ocean.

As a minimal model of the upper ocean, we examine the flow in a closed basin on a β plane using a quasi-geostrophic, reduced-gravity, linear model, driven by a prescribed wind stress. Resonances arise because eigenmodes are excited by time-dependent forcing at the eigenfrequencies of the basin. These basin free modes are analogous to those described by Pedlosky (1987) in a rigid-lid, homogeneous fluid.

The same basin modes are also responsible for low-frequency oscillations during the adjustment to Sverdrup balance with a steady wind from arbitrary initial conditions. The role of Rossby waves emanating from the eastern wall in establishing the interior flow is well understood in a semi-infinite geometry (Anderson and Gill 1975). If the wind is steady, Anderson and Gill (1975) indicate that the ocean interior adjusts with a single westward transit of the baroclinic Rossby waves. In a closed domain, the adjustment process is controlled by the interaction of the forced solution with the basin free modes, and the equilibrium solution is achieved through low-frequency, weakly damped basinwide oscillations, whose period is the transit time of long, first mode baroclinic Rossby waves.

The forced problem for a reduced-gravity or stratified fluid in a closed domain has received little attention because the analysis of basin modes is complicated by the constraint of total mass conservation, even in a basin of simple geometry. In the reduced-gravity case, Flierl (1977) and Larichev (1974), have examined the basin modes in a circular basin in the inviscid limit, but the time-dependent forced problem has not been considered in detail.

An analysis of the adjustment process in a reduced-gravity, shallow water layer, β-plane basin has been given by Milliff and McWilliams (1994). In those numerical calculations there is a suggestion of coupling between the short timescales of the coastal Kelvin waves generated by the mass adjustment process and the longer timescales of baroclinic Rossby waves, which mediate the interior vorticity adjustment. Capturing such mode coupling is computationally challenging because it requires long time integrations that can also resolve the short timescales. It is thus reassuring that Milliff and McWilliams (1994) find a close correspondence on long timescales between the shallow water dynamics, where

Corresponding author address: Paola Cessi, Scripps Institution of Oceanography, UCSD-0230, La Jolla, CA 92093-0230.
E-mail: pcessi@ucsd.edu

the rapid mass adjustment process is explicitly resolved, and the quasigeostrophic dynamics, where mass conservation is imposed as an integral constraint.

Here, we show that with weak dissipation, the often-ignored mass conservation constraint qualitatively changes the spectrum of the linear quasigeostrophic problem. Specifically, dissipation selects large-scale, low-frequency basin modes as the least damped eigenfunctions of the unforced problem, which are excited by forcing near the eigenperiods or during the adjustment process.

Evidence that such low-frequency oscillations are excited during adjustment, even with steady forcing, also comes from the numerical calculations of Cox (1987). He documents the periodic westward propagation of frontlike vertical displacements of the thermocline, at the speed of the first baroclinic mode. A new front emanates from the eastern boundary when the front in the previous period reaches the western boundary. However, as in Milliff and McWilliams (1994), the duration of the computations is too short to clearly discern a low-frequency, periodic signal.

2. Formulation

With the upper ocean in mind, we consider the quasigeostrophic potential vorticity equation for a single, reduced-gravity layer. The forcing is provided by the curl of the wind stress, curlτ, while dissipation by mesoscale eddies is parameterized as downgradient diffusion of potential vorticity, as recommended by Rhines and Young (1982). In the linear case, the evolution of the transport streamfunction, ψ, is governed by

$$(\nabla^2\psi - R^{-2}\psi)_t + \beta\psi_x = \rho^{-1}\,\mathrm{curl}\tau + \kappa\nabla^2(\nabla^2\psi - R^{-2}\psi). \quad (2.1)$$

In (2.1) $R = \sqrt{g'H}/f_0$ is the baroclinic deformation radius, and κ is the large-scale eddy diffusivity. As pointed out by McWilliams (1977) and Flierl (1977), in order to conserve the total mass of the layer, one should enforce the conditions

$$\psi|_{\text{boundary}} = \psi_0(t), \qquad \int_{\text{area}} \psi\, dx\, dy = 0, \quad (2.2)$$

rather than the ''incorrect'' boundary condition

$$\psi|_{\text{boundary}} = 0. \quad (2.3)$$

The latter condition is incorrect because in general the total mass in the layer is not conserved if (2.1) is integrated with (2.3) as a boundary condition.

Additional conditions must be specified because of the fourth-order dissipation operator, and here we require that the tangential velocity vanishes on the boundaries (no slip).

The boundary conditions and integral constraint in (2.2) ensure that the total mass in the layer is conserved, by requiring that the area-averaged depth of the layer is equal to H at all times. This means that we adopt the convention that any initial condition on ψ must also have zero average. That the boundary pressure is independent of position and fluctuates in synchrony along the basin's perimeter, comes from the timescale separation between the slow quasigeostrophic motion and the rapid ageostrophic flow. Therefore, the boundary condition (2.2) ''parameterizes'' all those rapid ageostrophic motions that readjust the mass balance, such as the Kelvin waves and the Poincaré modes.

In the linear case examined here, the streamfunction of the reduced-gravity model (2.1), with boundary conditions (2.2), obeys the same dynamics as each baroclinic component of a vertical modal projection of $\psi(x, y, z, t)$ in a continuously stratified model without bottom relief [Anderson and Gill 1975; Pedlosky 1987 (chapter 6.12)]. Thus, as long as the appropriate modal deformation radius is used in the definition of R, our results apply to a larger class of general circulation models.

For planetary basins, there is a large-scale separation between the baroclinic deformation radius, R, and the width of the basin, L_x. To illustrate this, we nondimensionalize (2.1), using the following variables

$$(x, y) = L_x(\hat{x}, \hat{y}), \qquad t = t_0\hat{t}, \qquad \psi = \tau_0(\beta\rho)^{-1}\hat{\psi}. \quad (2.4)$$

Time has been scaled by the transit time of long Rossby waves, t_0, defined as

$$t_0 \equiv L_x/(\beta R^2); \quad (2.5)$$

t_0 is of the order of decades for midlatitude planetary basins.

Here τ_0 is the amplitude of the wind stress, and the dimensional wind stress curl is given by

$$\mathrm{curl}\tau = \tau_0 G(x, y, t)/L_x, \quad (2.6)$$

with G a nondimensional function with maximum amplitude of one.

With the choice (2.4) the evolution of the streamfunction in nondimensional units is given by (after dropping the carets):

$$(\epsilon\nabla^2\psi - \psi)_t + \psi_x = G(x, y, t) + \delta\nabla^2(\epsilon\nabla^2\psi - \psi). \quad (2.7)$$

On the boundaries, located at $x = 0, 1$ and $y = 0, L_y/L_x$, we enforce

$$\psi = \psi_0(t), \qquad \epsilon\delta\nabla\psi\cdot\mathbf{n} = 0, \quad (2.8)$$

subject to the constraint

$$\int_0^1 dx \int_0^r \psi\, dy = 0, \quad (2.9)$$

where $r \equiv L_y/L_x$ is the aspect ratio of the basin. Two small parameters emerge from this nondimensionalization:

$$\epsilon \equiv (R/L_x)^2, \qquad \delta \equiv \kappa/(\beta L_x R^2). \quad (2.10)$$

Here ϵ measures the importance of inertia versus vortex stretching and δ is the ratio of the damping time of a long Rossby wave and its basin-crossing time. In the middle latitudes typical values of the dimensional scales are

$$\beta = 2 \times 10^{-11}\ \mathrm{m^{-1}\ s^{-1}}, \quad L_x = 0.8 \times 10^7\ \mathrm{m},$$
$$R = 3 \times 10^4\ \mathrm{m}, \quad \kappa = 1000\ \mathrm{m^2\ s^{-1}}. \quad (2.11)$$

Thus both ϵ and δ are very small, but $\epsilon \ll \delta$ because using the values in (2.11) we get

$$\epsilon = 2.4 \times 10^{-5}, \quad \delta = 6.9 \times 10^{-3}. \quad (2.12)$$

Before solving for the forced problem, we examine the eigenspectrum of the homogenous problem associated with (2.7) in the limit $\epsilon \ll \delta$, and compare it with that obtained in the inviscid limit $\delta = 0$.

3. Weakly dissipated basin modes

Flierl (1977) has discussed the free basin modes in the inviscid case ($\delta = 0$) and concluded that there are no qualitative differences between the two boundary conditions (2.2) and (2.3). In this section we show that, when dissipation is gradually increased, selected low-frequency modes are singled out by friction as the least damped basin modes, *only* with the mass-conserving boundary condition. Moreover, as long as ϵ is not larger than δ, the effect of inertia is negligible on the least damped basin modes.

We thus solve for the free basin modes of the unforced problem associated with (2.7), by assuming that $\psi = \exp(-i\omega t)\phi(x, y)$, with ϕ determined by

$$-i\omega[\epsilon\nabla^2\phi - \phi] + \phi_x = \delta\nabla^2(\epsilon\nabla^2\phi - \phi). \quad (3.1)$$

The boundary conditions are (2.8) and the integral constraint (2.9).

To numerically approximate the basin modes, we discretize the pressure, ϕ, onto a regular lattice with $N_x \times N_y$ unknowns at each grid point in the interior of the basin and one additional unknown for the boundary pressure, ϕ_o. A finite difference approximation of (3.1) at each of the interior grid points, together with a discretization of the integral constraint (2.9), yields $N_x \times N_y + 1$ equations for an equal number of unknowns. In discretized form, these equations form a generalized eigenvalue problem with eigenvalue, ω, of the form

$$-i\omega\mathbf{B}\phi = \mathbf{A}\phi. \quad (3.2)$$

Second-order accurate centered difference approximations yield matrices **A** and **B**, which have a nearly banded structure, except for the necessity to reference a single unknown for the boundary pressure in each of the discretized equations for the two rows of grid points adjacent to the boundary. In addition, the integral constraint—approximated using the trapezoidal rule—yields one dense row in **A** and a corresponding row with all zero entries in **B**, so the latter matrix is singular.

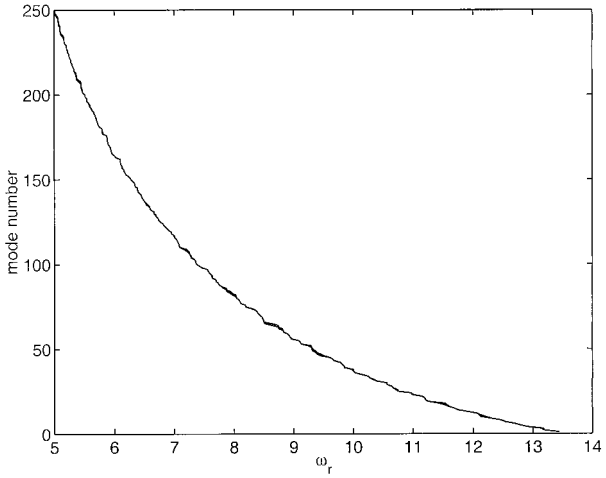

FIG. 1. Plot of the largest 250 eigenvalues in the inviscid, inertial case, $\delta = 0$, $\epsilon = 1.25 \times 10^{-3}$ for the mass-conserving (2.2) and incorrect (2.3) boundary conditions. The frequency is the abscissa, and the ordinate an arbitrary mode number. All eigenvalues are real, and there are actually two curves on the graph.

Despite the complications associated with the integral constraint, **A** and **B** are sparse, so it is possible to take advantage of a sparse matrix eigenvalue solver. We used shifted Arnoldi iterations as implemented in MATLAB's sparse matrix package. For the results presented below, we typically used $N_x = 95$ grid points in the x direction and $N_y = 95$ grid points in the y direction. We also have verified that increasing the resolution produces little quantitative change in the weakly damped part of the spectrum.

For comparison we also compute the eigenspectrum using the incorrect boundary condition (2.3) and no slip. Figure 1 shows the spectrum of the eigenvalues in the inviscid case, $\delta = 0$, and with $\epsilon = 1.25 \times 10^{-3}$, for both sets of boundary conditions. The value of ϵ is much larger than the oceanographically relevant one, but the latter is computationally too demanding. The two curves are essentially indistinguishable, confirming the result of Flierl (1977), obtained for a circular basin, that the mass-conserving condition does not alter the basin-mode spectrum in the inviscid case. However, dissipation changes the picture qualitatively: Fig. 2 shows the eigenspectra of (3.1) for both boundary conditions (the eigenvalues for the correct boundary condition are marked by circles while those for the incorrect boundary condition are marked by crosses). A few selected modes with the mass-conserving boundary conditions are promoted by dissipation to the special status of weakly damped, while a few modes of the mass-conserving eigenspectrum are heavily penalized by friction. In contrast, none of the modes with the incorrect boundary condition are either promoted or demoted: all of them have a damping rate that decreases with modal frequency, as expected for Rossby waves where the frequency is inversely proportional to the wavenumber.

Examination of the spatial structure of the viscously

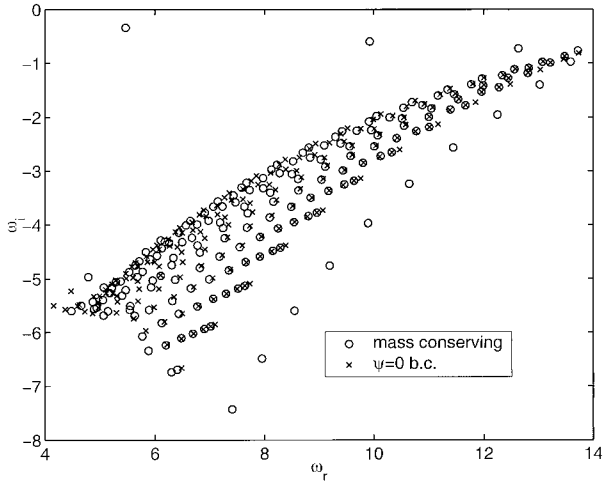

FIG. 2. Scatterplot of some eigenvalues in the weakly dissipative limit, $\delta = 1 \times 10^{-3}$, $\epsilon = 1.25 \times 10^{-3}$, for the mass conserving (circles) and incorrect (crosses) boundary conditions. The imaginary part is the ordinate, and the real part the abscissa.

promoted modes, reveals that, in the inviscid case, they are characterized by a mixture of small and large scales (top panels of Figs. 3 and 4). The large-scale component is completely missing in the modes with neighboring frequencies and in the modes with the same frequency for the incorrect boundary condition. Figure 3 shows the least-damped eigenfunction obtained with dissipation (lower panels) and the eigenfunction for the same mode without dissipation (top panel). The middle panels show the eigenfunction of the same mode for an intermediate value of viscosity; that is, $\delta = 3 \times 10^{-4}$. Figure 4 shows the second least damped mode from Fig. 2 (bottom panels), its inviscid ancestor (top panels), and the intermediate mode at $\delta = 3 \times 10^{-4}$ (middle panels). Although the frequency slightly changes with dissipation, it is possible to follow each eigenmode individually as a function of δ. Figure 5 shows the real (top) and imaginary (bottom) part of two eigenvalues as a function of the frictional parameter δ for fixed $\epsilon = 1.25 \times 10^{-3}$. The promoted eigenvalue (solid line) experiences very little damping as δ is increased and the corresponding eigenfunction is shown in Fig. 3. The other eigenvalue (dashed line), whose eigenfunction has a spatial structure in the inviscid case (not shown) similar to that in the top panel of Fig. 3, suffers much damping when $\delta \neq 0$.

In summary, when $\delta \geq O(\epsilon)$, dissipation homogenizes the frictionally promoted eigenfunctions, destroying the small-scale structures except near the western boundary, while leaving the large-scale structure essentially intact.

Because dissipative scale selection is the essential ingredient for the segregation of basin modes, it is important to verify which results are robust to changes in the form of friction. Therefore, we repeated some calculations of the eigenspectrum omitting the fourth-order diffusion term on the right-hand side of (3.1): this is

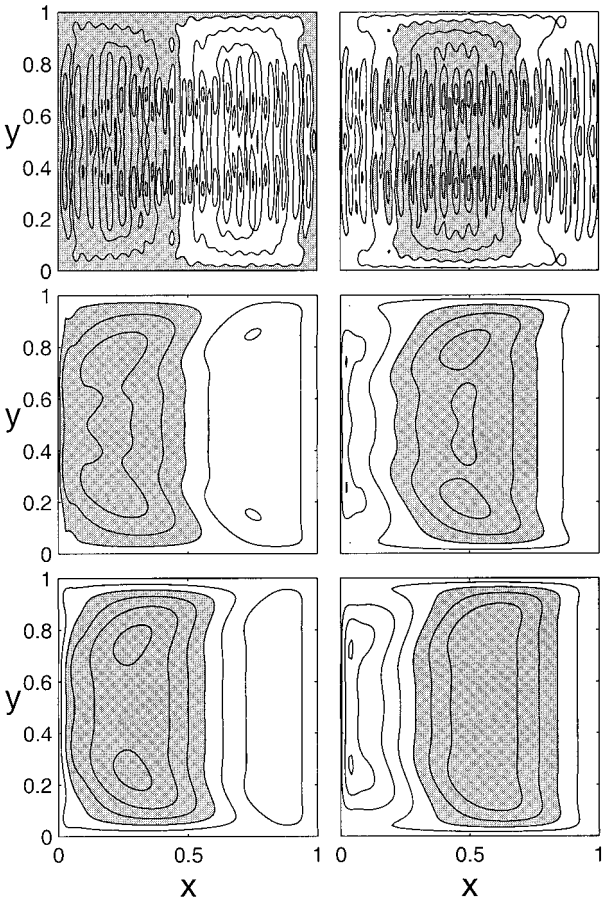

FIG. 3. The real and imaginary part of the eigenfunction corresponding to the least damped eigenmode of Fig. 2 are contoured (bottom); the eigenvalue is $\omega = 5.468 - 0.339i$, for $\delta = 1 \times 10^{-3}$. The real and imaginary part of the eigenfunction corresponding to the same mode in the inviscid case are contoured (top); the eigenvalue is $\omega = 5.537$. The middle panels show the real and imaginary part of the least-damped eigenfunction for $\delta = 3 \times 10^{-4}$, whose corresponding eigenvalue is $\omega = 5.484 - 0.230i$. All eigenfunctions satisfy the mass-conserving boundary conditions, and negative values are shaded.

the term proportional to the product $\delta\epsilon$. In this way, only the boundary conditions (2.2) can be enforced, but not the no-slip constraint. For reference, we also calculate the eigenspectrum using the boundary condition (2.3), which does not conserve mass. The eigenspectra are shown in Fig. 6 for $\delta = 5 \times 10^{-3}$ and $\epsilon = 1.25 \times 10^{-3}$ (the eigenvalues for the mass-conserving boundary condition are marked by circles while those for the boundary condition that does not conserve total mass are marked by crosses). The qualitative distinction between modes that are heavily damped and modes that are frictionally promoted does not differ from that obtained with higher-order viscosity, although the quantitative separation of the damping rates is not as large as that obtained with dissipation that is more scale selective (cf. the ordinates of Fig. 2, where $\delta = 1 \times 10^{-3}$, and Fig. 6, where $\delta = 5 \times 10^{-3}$). In Fig. 6, we also

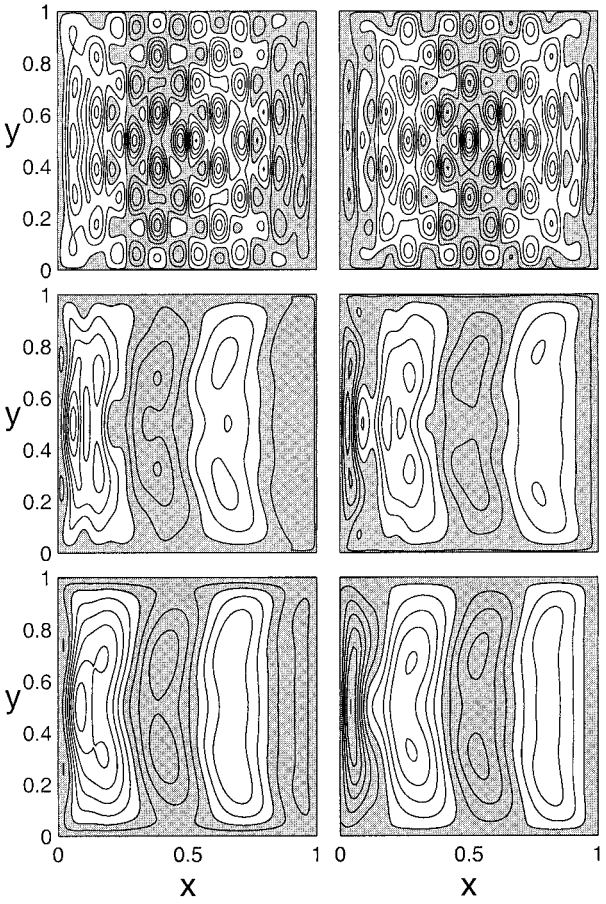

FIG. 4. The real and imaginary part of the eigenfunction corresponding to the second least-damped eigenmode of Fig. 2 are contoured (bottom); the eigenvalue is $\omega = 9.923 - 0.596i$, for $\delta = 1 \times 10^{-3}$. The real and imaginary part of eigenfunction corresponding to the same mode in the inviscid case are contoured (top); the eigenvalue is $\omega = 9.917$. The middle panels show the real and imaginary part of the same eigenfunction for $\delta = 3 \times 10^{-4}$, whose corresponding eigenvalue is $\omega = 9.915 - 0.403i$. All eigenfunctions satisfy the mass conserving boundary conditions, and negative values are shaded.

plot the three least damped eigenvalues obtained without inertia, $\epsilon = 0$ (they are marked by squares). The difference between the least damped eigenvalues for $\epsilon = 0$ and $\epsilon = 1.25 \times 10^{-3}$ is a small percentage of the frequency, and increases with mode number. Specifically, with $\epsilon = 1.25 \times 10^{-3}$, the maximum frequency attainable is about 13.5. However, as $\epsilon \to 0$, and more Rossby deformation radii fit in the basin more frictionally promoted modes emerge with progressively higher frequencies. More importantly, Fig. 7 shows that with low-order friction the eigenfunctions of the least-damped eigenmodes, both with and without inertia, have the same spatial structures as those obtained with higher-order dissipation, shown in the bottom panels of Figs. 3 and 4.

Thus, the frictionally promoted eigenmodes are not sensitive to the specific form of friction and are only marginally affected by inertia in the oceanographically relevant regime where $\epsilon \ll \delta$.

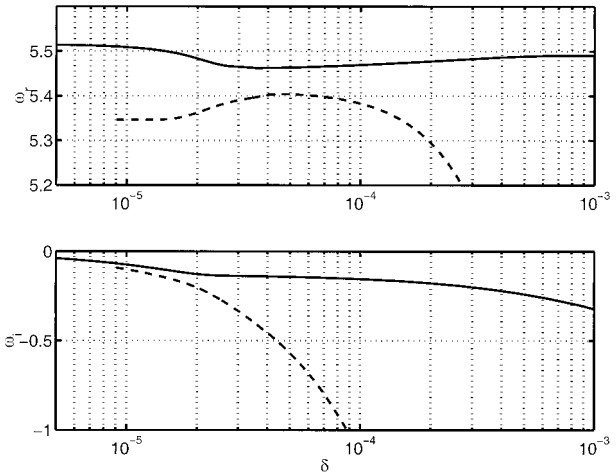

FIG. 5. The (a) real and (b) imaginary part of two eigenvalues, as a function of δ for $\epsilon = 1.25 \times 10^{-3}$. The solid line corresponds to the eigenvalue whose eigenfunction is displayed in Fig. 3. The dashed line corresponds to another eigenvalue that experiences much more damping as δ is increased, although its eigenfunction has, in the inviscid limit, a spatial structure similar to that shown in the top panel of Fig. 3.

a. Energetics

Although a complete analytical description of the inviscid modes with mass-conserving boundary conditions is not possible, some insight into the difference between the two boundary conditions (2.2) and (2.3) is obtained by examining the energy balance. Multiplying (2.7) by ψ gives the evolution of energy density:

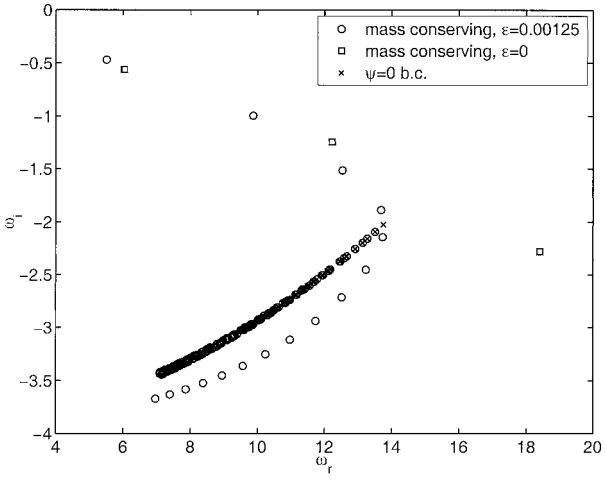

FIG. 6. Scatterplot of some eigenvalues with dissipation in the form of Rayleigh friction, i.e., without the fourth-order term on the rhs of (3.1) proportional to $\epsilon\delta$; $\delta = 5 \times 10^{-3}$, $\epsilon = 1.25 \times 10^{-3}$, for the mass conserving (circles), and incorrect (crosses) boundary conditions. Also shown is the case where inertia is omitted, $\epsilon = 0$, with mass conserving boundary conditions (squares).

$$E_t = -\nabla \cdot \mathbf{F} - \psi G - D, \tag{3.3}$$

where

$$E \equiv [\epsilon \nabla\psi \cdot \nabla\psi + \psi^2]/2,$$
$$\mathbf{F} \equiv -\psi[\epsilon \nabla\psi_t + \hat{\mathbf{x}}\psi/2 + \delta\nabla(\psi - \epsilon\nabla^2\psi)] - \delta\epsilon\nabla\psi\nabla^2\psi,$$
$$D \equiv \delta[(\nabla\psi)^2 + \epsilon(\nabla^2\psi)^2]. \tag{3.4}$$

Conservation of total energy is obtained by integrating (3.3) over the domain. Assuming either no-slip or free-slip ($\delta\epsilon\nabla^2\psi = 0$) on the boundaries, we obtain

$$\int_{\text{area}} E_t \, dx \, dy = \psi_0 \oint_{\text{boundary}} [\epsilon\nabla\psi_t + \delta\nabla(\psi - \epsilon\nabla^2\psi)] \cdot \hat{\mathbf{n}} \, dl - \int_{\text{area}} [\psi G + D] \, dx \, dy. \tag{3.5}$$

The first term on the right-hand side is the flux of energy into the boundary. It simplifies considerably because, integrating the vorticity equation, (2.7), over the domain and using (2.2), one obtains

$$\oint_{\text{boundary}} [\epsilon\nabla\psi_t + \delta\nabla(\psi - \epsilon\nabla^2\psi) \cdot \mathbf{n} \, dl = \int_{\text{area}} G \, dx \, dy. \tag{3.6}$$

So, finally

$$\int_{\text{area}} E_t \, dx \, dy = -\int_{\text{area}} [(\psi - \psi_0)G + D] \, dx \, dy. \tag{3.7}$$

The formulation (3.5) reveals that with the incorrect boundary condition, (2.3), the flux of energy, $\mathbf{F} \cdot \mathbf{n}$, vanishes *at every point on the boundary,* so there is no flux of energy into the boundary. As discussed in Pedlosky (1987), this implies that Rossby waves incident on the western boundary must be reflected with equal and opposite energy flux. Because the wavelength is shortened below the Rossby deformation radius upon reflection from a western boundary, dissipation is very effective at removing energy there.

However, with the mass-conserving boundary condition, (2.2), the normal component of the energy flux vector does not vanish pointwise on the boundary. Instead, when integrated along the whole arclength, it is proportional to the net vorticity input. Specifically, in the case of free basin modes, where $G = 0$, the boundary average of $\mathbf{F} \cdot \mathbf{n}$ vanishes, implying that some energy can be redistributed along the boundary by the parameterized ageostrophic motion, which is also responsible for the mass rearrangement. Presumably, the modes that are viscously promoted have an especially large fraction of energy that is transmitted along the boundary and a small fraction that is directly reflected into waves shorter than the deformation radius.

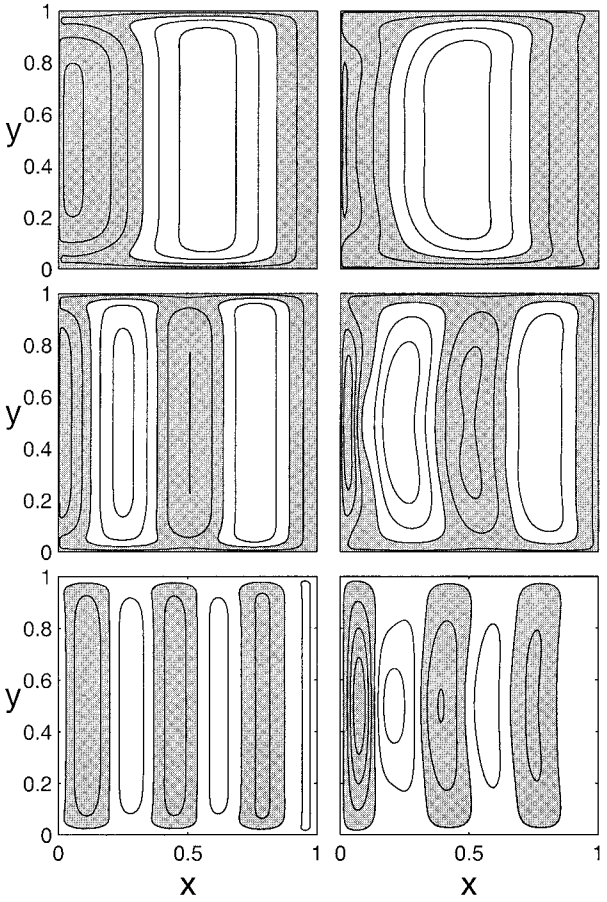

FIG. 7. The imaginary parts of the eigenfunctions corresponding to the three least-damped eigenmodes of Fig. 6 for $\epsilon = 0$ (left) and for $\epsilon = 1.25 \times 10^{-3}$ (right). The eigenvalues are: $\omega = 6.0 - 0.55i$ (top left), $\omega = 5.5 - 0.47i$ (top right); $\omega = 12.2 - 1.2i$ (middle left), $\omega = 9.9 - 1i$ (middle right); $\omega = 18.3 - 2.3i$ (bottom left), $\omega = 12.5 - 1.5i$ (bottom right). All eigenfunctions satisfy the mass-conserving boundary conditions, and negative values are shaded.

b. Summary

Large-scale, low-frequency modes emerge from the inviscid spectrum with the gradual addition of weak dissipation, and their structure is robust to the specific form of friction. Moreover, as long as ϵ is not larger than δ, the role of inertia is marginal and it does not qualitatively alter the frictionally promoted modes, while friction very much alters some modes of the inertial, inviscid spectrum.

Thus it is reasonable to neglect inertia but not dissipation for basinwide flows, so we proceed to examine the effect of using the boundary conditions plus integral

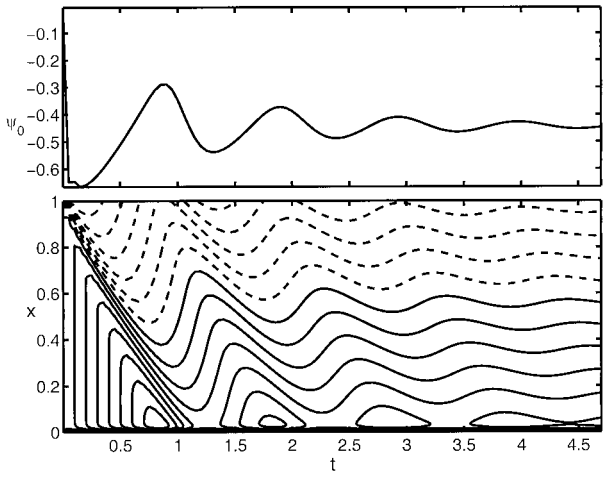

FIG. 8. Plot of the nondimensional boundary streamfunction, solution of (3.8), as a function of time, for $G = -1$, $\delta = 7 \times 10^{-3}$, $\epsilon = 0$, and $L_y = L_x$ (upper panel). The streamfunction, ψ, at the latitude $y = 0.5$, is contoured as a function of time and longitude x (lower panel) with a contour interval of 0.01 (negative contours are dashed). Time is in units of t_0, defined in (2.5), and x is in units of the basin width, L_x.

constraint (2.2) rather than the more commonly used boundary condition (2.3) for the simplified forced problem,

$$-\psi_t + \psi_x = G(x, y, t) - \delta\nabla^2\psi. \tag{3.8}$$

4. The initial value problem

A simple illustration of the role of the low-frequency eigenspectrum when using the mass-conserving versus non-mass-conserving boundary conditions, is obtained when considering the adjustment of a stratified ocean, initially at rest, to a constant wind stress curl. We thus solve (3.8) subject to the initial condition $\psi = 0$, with $G = -1$. This is the same problem considered by Anderson and Gill (1975) except that we conserve mass.

a. A simple example

For a steady wind stress curl, a steady state is eventually reached because of friction. However, the final equilibrium is approached through a weakly damped oscillation. The approach to the steady state is illustrated in Fig. 8, where the streamfunction at $y = 1/2$ is contoured as a function of time and longitude in the lower panel. A progressively weakening front is initially generated at the eastern boundary and then propagates westward. As the front reaches the western wall, a new front starts from the eastern boundary, and the cycle repeats with a weaker amplitude. Each period is analogous to the adjustment process considered by Anderson and Gill (1975), but here the cycle is repeated many times. The arrival of each front at the western boundary coincides with a maximum in the boundary streamfunction $\psi_0(t)$, plotted in the upper panel. The nondimensional period of the damped oscillation is one, which corresponds to the long Rossby wave transit time t_0, given in (2.5).

The spatial structure of the flow is illustrated in Fig. 9, which shows four snapshots of the anomaly of the dynamical streamfunction, $\psi - \psi_0$. The anomaly is defined as the difference between the value of the function at a given time and the final steady state, which is shown in Fig. 10. The streamfunction anomaly takes the form of a basin mode propagating toward the western boundary at the speed of the long, baroclinic Rossby waves: it is the inertialess limit of the least damped, lowest frequency eigenmode described in section 3 (cf. Figs. 7 and 3).

To understand this damped-oscillatory solution it is useful to examine the one-dimensional dynamics, valid in the center of the gyre, outside the frictional boundary layers to the north and south walls.

b. One-dimensional approximation

Away from the viscous boundary layers to the north and south it is possible to neglect the term ψ_{yy} and neglect the boundary conditions on the northern and southern walls. When $G = -1$, we seek a solution of the form

$$\psi = \psi_f(x) + \psi_h(x, t). \tag{4.1}$$

The forced solution, ψ_f, is

$$\psi_f = [1/2 - x - \exp(-x/\delta)] + O(\delta). \tag{4.2}$$

The arbitrary constant in the forced solution has been chosen so that, to leading order in δ, ψ_f has zero average. With this choice, ψ_f coincides with the final steady state, and it is an approximation, valid outside the north and south boundary layers, of the solution shown in Fig. 10. Therefore, the one-dimensional model predicts that the final value of the boundary streamfunction is approximately -0.5, in good agreement with the numerical solution shown in Fig. 8, which equilibrates to -0.45.

In order to satisfy the initial conditions we must add a solution of the homogeneous problem, ψ_h. The general solution of the homogeneous, y-independent problem associated with (3.8), that satisfies the boundary conditions (2.2), is

$$\psi_h = \sum_{n=0}^{\infty} \exp(-4\pi^2 n^2 \delta t) \times [a_n \cos 2\pi n(x + t) + b_n \sin 2\pi n(x + t)]. \tag{4.3}$$

The terms in the series are the interior approximation of the basin modes described in section 3, in the limit of no inertia (e.g., the left panels of Fig. 7). The coefficients a_n and b_n are determined by enforcing the initial condition

$$\psi(x, t = 0) = \psi_f \sum_{n=1}^{\infty} [a_n \cos 2\pi nx + b_n \sin 2\pi nx]. \tag{4.4}$$

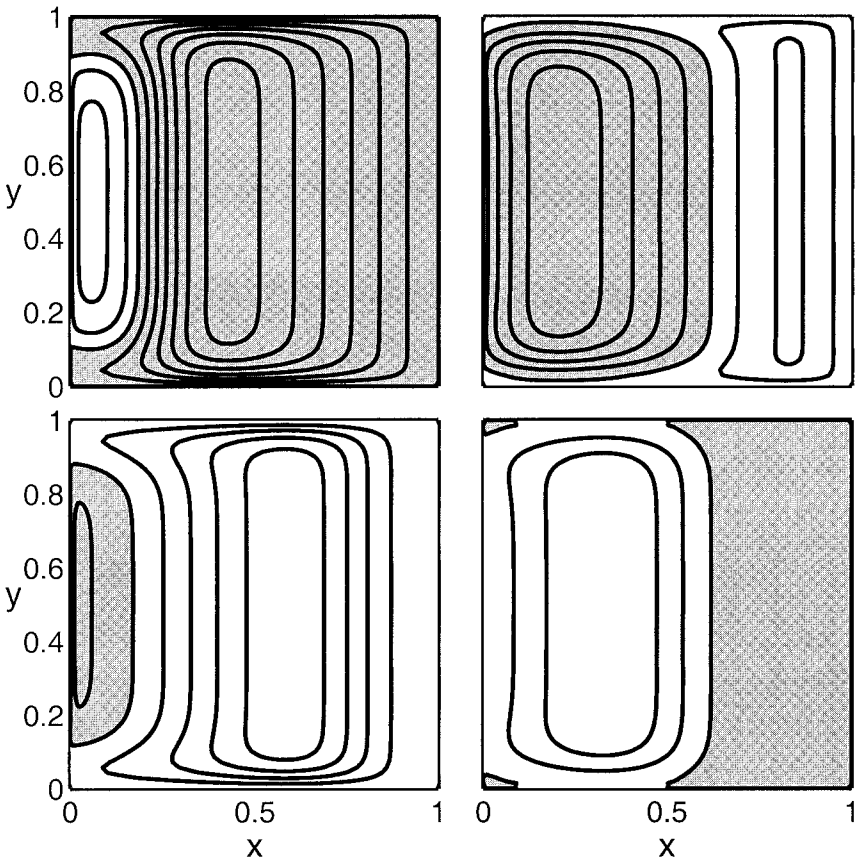

FIG. 9. Departures of the dynamical streamfunction, $\psi - \psi_0$, from the final steady state, at four selected times: (upper left) at $t = 0.8$, (upper right) at $t = 1.05$, (lower left) at $t = 1.3$, and (lower right) at $t = 1.55$. The transport anomalies are almost independent of latitude away from meridional boundary layers, and are of large scale. The contour interval is 0.05 and negative values are shaded. All the other parameters are as in Fig. 8.

Because $\cos 2\pi nx$ and $\sin 2\pi nx$ form a complete set for the functions with zero average, any such initial condition can be applied.

The period of the gravest mode for the homogenous solution, in this nondispersive, long-wave limit, is one, that is, given by the Rossby wave transit time, t_0, in dimensional units. The wavelength of the gravest and least damped mode is one, that is, the width of the basin, L_x, in dimensional units. Each mode is characterized by a traveling wave with quantized wavenumber, $2\pi n$, and frequency, $-2\pi n$. The decay rate increases with mode number and is given by $4\pi^2 n^2 \delta$, that is, very small for planetary basins as long as the mode number is moderate. Therefore, the grave modes in (4.3) decay very slowly. The one-dimensional approximation thus captures well the period of the basin modes as well as their interior shape, shown in Fig. 7 for the two-dimensional numerical solution.

c. A further approximation

The solution (4.1) with (4.2) and (4.3) illustrates that the period of these basin modes is much shorter than the decay time, so friction can be neglected for times of the order of a few periods except in thin boundary layers. It is thus possible to construct the interior solution by neglecting friction completely. We thus consider the solutions of the inviscid problem associated with (3.8),

$$-\psi_t + \psi_x = G(x, y, t). \tag{4.5}$$

In the inviscid limit we can only expect to enforce the boundary condition $\psi = \psi_0(t)$ on the eastern boundary $x = 1$, but we can still apply the mass conservation constraint in (2.9) because the return flow on the other three boundaries occurs in thin boundary layers.

We look for a solution of the form

$$\psi = \psi_f + \psi_h(x + t), \tag{4.6}$$

where ψ_h satisfies the homogeneous equation and ψ_f is the forced solution. The inviscid problem (4.5) is a hyperbolic equation, whose characteristics are given by

$$x + t = C. \tag{4.7}$$

For $C < 1$, the characteristics intersect the initial data along $\{t = 0, 0 < x < 1\}$, while for $C > 1$, they intersect

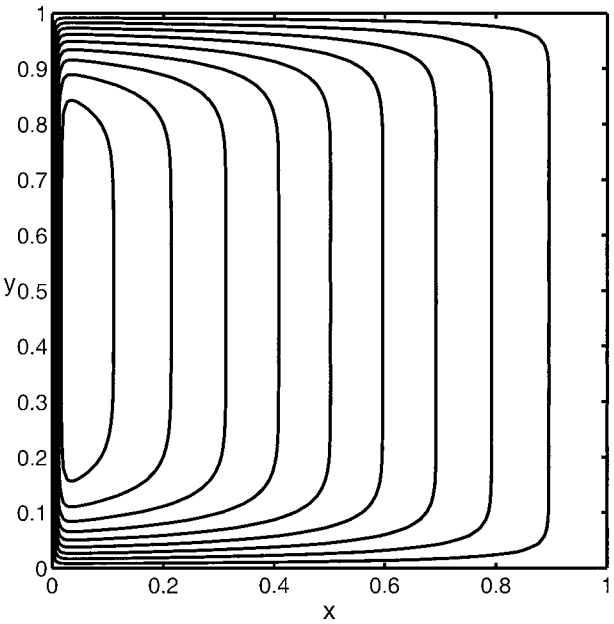

FIG. 10. The dynamical streamfunction, $\psi - \psi_0$, at the end of the calculation described in section 4a, when the Sverdrup equilibrium is essentially reached, that is, $t = 4.75$. The contour interval is 0.5 and all the parameters are as in Fig. 8.

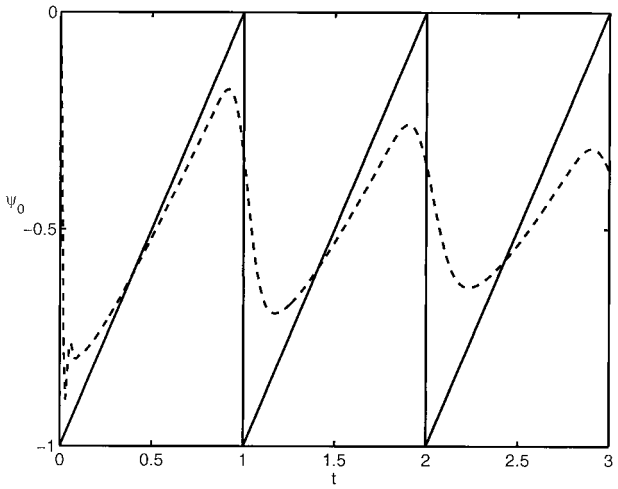

FIG. 11. The boundary streamfunction, ψ_0 in the inviscid, one-dimensional approximation, valid for times much shorter than the decay time (solid line). The dashed line shows ψ_0 computed by solving the two-dimensional, frictional problem (3.8) with $\delta = 1.5 \times 10^{-3}$, and all the other parameters are as in Fig. 8. The period is well captured by the inviscid, one-dimensional approximation, as is the relaxation-oscillation character of the solution.

the eastern boundary along $\{x = 1, t > 0\}$. We require that the initial condition $\psi = \psi_I(x)$ and the boundary data, $\psi = \psi_0(t)$ on the eastern wall, are satisfied by the homogeneous solution, which is then given by

$$\psi_h(x + t) = \begin{cases} \psi_I(x + t) & \text{for } x + t < 1 \\ \psi_0(x + t - 1) & \text{for } x + t > 1. \end{cases} \quad (4.8)$$

Since the initial and boundary conditions are satisfied by ψ_h, the forced solution must vanish at $t = 0$ and at $x = 1$, and for the specific case where G is only a function of y, it is given by

$$\psi_f = \begin{cases} -tG & \text{for } x + t < 1 \\ (x - 1)G & \text{for } x + t > 1. \end{cases} \quad (4.9)$$

To determine the unknown boundary pressure, $\psi_0(s)$, we apply the mass conservation constraint, (2.9). For $t < 1$, in the specific case where $\psi_I = 0$, mass conservation leads to

$$\int_0^r dy \left\{ \int_0^{1-t} -tG\, dx + \int_{1-t}^1 [(x - 1)G + \psi_0(x + t - 1)]\, dx \right\} = 0, \quad (4.10)$$

which simplifies to

$$\int_0^t \psi_0(s)\, ds = \frac{(2t - t^2)}{2r} \int_0^r G\, dy. \quad (4.11)$$

By differentiating (4.12) with respect to t, we obtain the solution for $t < 1$:

$$\psi_0(t) = \frac{(1 - t)}{r} \int_0^r G\, dy. \quad (4.12)$$

For $t > 1$, the mass conservation constraint yields

$$\int_0^r dy \int_0^1 [(x - 1)G + \psi_0(x + t - 1)]\, dx = 0, \quad (4.13)$$

which simplifies to the integral equation

$$\int_{t-1}^t \psi_0(s)\, ds = \frac{1}{2r} \int_0^r G\, dy. \quad (4.14)$$

The solution of (4.15) can be obtained by differentiating with respect to t. Using Leibnitz rule we find

$$\psi_0(t) - \psi_0(t - 1) = 0. \quad (4.15)$$

Therefore, ψ_0 is periodic in time for $t > 1$, with period equal to one, and the solution (4.13) obtained in the initial period, $0 < t < 1$, is repeated thereafter. In summary the boundary pressure can be written as

$$\psi_0(t) = \frac{(n - t)}{r} \int_0^r G\, dy \quad \text{for } n < t < n + 1. \quad (4.16)$$

Figure 11 shows $\psi_0(t)$ in the case where $G = -1$, and $L_y = L_x$ (solid line). The oscillation around the value $-1/2$ should be compared with the numerical result for finite friction (dashed line). In the frictional case, the oscillation is damped and even the initial amplitude is smaller than that predicted by (4.12). However, comparison with the top panel of Fig. 8, which has a larger

value of δ, shows that the amplitude of the initial pulse approaches -1, as the friction is decreased.

The solution (4.16), illustrates that, on the β plane the amplitude of the oscillation is proportional to the area-averaged wind stress curl, that is, to the net Ekman pumping. At least in the case where the long Rossby wave speed is constant, the oscillation is absent if there is no net mass injection from the Ekman layer. Also, the inviscid solution shows that the periodic solution is in the form of a sawtooth-oscillation triggered by the arrival at the western boundary of the Rossby wave front separating the local response to the wind stress curl (4.9a) from the flow in time-dependent Sverdrup balance (4.9b). The adjustment of the boundary pressure provides a continuous source of Rossby waves emanating from the eastern boundary. In turn, the arrival of the long Rossby waves at the western boundary provides a continuous source of time dependence of the boundary pressure, and steady state is not reached in the interior in the inviscid limit. In the interpretation offered by Milliff and McWilliams (1994), the boundary pressure, ψ_0, represents the effect of mass readjustment performed by fast ageostrophic motions such as Kelvin waves. Kelvin waves are continuosly excited by the arrival of the Rossby waves at the western boundary. In turn, when the Kelvin waves reach the eastern boundary, that is, instantly in the quasigeostrophic limit, more Rossby waves are excited and the cycle repeats.

5. Resonances

Given that the homogenous solution (4.3) is a damped oscillation, it is not surprising that time-dependent forcing at the resonant frequency gives rise to a large amplitude response. To illustrate the resonant response, we consider the solutions of (4.5) when the forcing is periodic in time. As an example we solve

$$\psi_t - \psi_x = -A \sin\omega t, \tag{5.1}$$

with A a constant. The boundary conditions are the same as those in section 4c, so mass conservation is guaranteed. The forced solution, neglecting the transient part related to the application of the initial condition, is

$$\psi = A\omega^{-1} \cos\omega t + A \frac{\sin\omega(t + x - 1) - \sin\omega(t + x)}{2(1 - \cos\omega)}. \tag{5.2}$$

Without friction, the response is infinite for the resonant frequencies, $\omega = 2\pi n$. The mass conserving solution, (5.2), should be compared to the forced response obtained solving (5.1), but with the traditional boundary condition $\psi = 0$ at $x = 1$. In this case the solution is

$$\psi = A\omega^{-1}[\cos\omega t - \cos\omega(t + x - 1)], \tag{5.3}$$

and there is no frequency that gives rise to a resonant response.

With friction, the response at the resonant frequency is large but finite. Figure 12 shows time–longitude plots of the dynamical streamfunction, $\psi - \psi_0$, solutions of (3.8) for a forcing with period one. The function is evaluated at the midbasin latitude, $y = r/2$, and we show the results for both boundary conditions, (2.2) and (2.3). Although the structure is the same in the two cases, the value of the amplitude is larger by over a factor of 10 when the mass-conserving condition is enforced (left panel). Moreover, the amplitude of the response for the mass-conserving boundary condition increases as friction is reduced (not shown), while this is not the case if (2.3) is used. Therefore, with friction, a large response is obtained for selected, quasi-resonant frequencies.

6. Discussion

We have shown that low-frequency, weakly dissipated basin modes are viscously selected in a reduced-gravity ocean on a β plane. Because of these modes the adjustment to Sverdrup balance with a steady wind is slow and many oscillations around the final steady state occur. If the wind has a time-dependent component, an amplified response is obtained at the resonant frequencies.

Essential to the viscously promoted modes is the mass-conserving boundary condition (2.2) instead of the incorrect one (2.3). The condition (2.2) on the boundary pressure parameterizes the rapid ageostrophic motion responsible for the mass rearrangement within the fluid. In the process of redistributing the mass, the boundary pressure also moves some energy from the western to the eastern boundary through a nonlocal process, which avoids the direct cascade to small scales inherent in the reflection of Rossby waves at a western boundary. This transfer is instantaneous in the quasigeostrophic approximation. In shallow water dynamics, it is just much more rapid than the baroclinic Rossby wave transit time, at least in the middle latitude.

The modes just described are the midlatitude analog of the equatorial basin modes described by Cane and Sarachick (1977) and Cane and Moore (1981). In the tropical waveguide these basin modes are the result of Kelvin waves being reflected as long Rossby waves on the eastern boundary and long Rossby waves being reflected as Kelvin waves on the western boundary. As in the midlatitudes, these equatorial mixed Kelvin–Rossby wave basin modes lead to a slow oscillatory adjustment to changes in the winds. Because, at the equator, the propagation time of the Kelvin wave is only a factor of 3 above that of the fastest baroclinic Rossby wave, both motions must be explicitly resolved.

In both equatorial and midlatitude regions, the frequency of these mixed modes is a multiple of $2\pi/t_0$, where t_0 is the long Rossby wave transit time. However, at the equator the transit time is of the order of ten months, while in midlatitudes it is of the order of decades. Thus it is not clear what the period for basin modes that span a whole hemisphere would be. Preliminary calculations using (2.1) with a latitudinally vary-

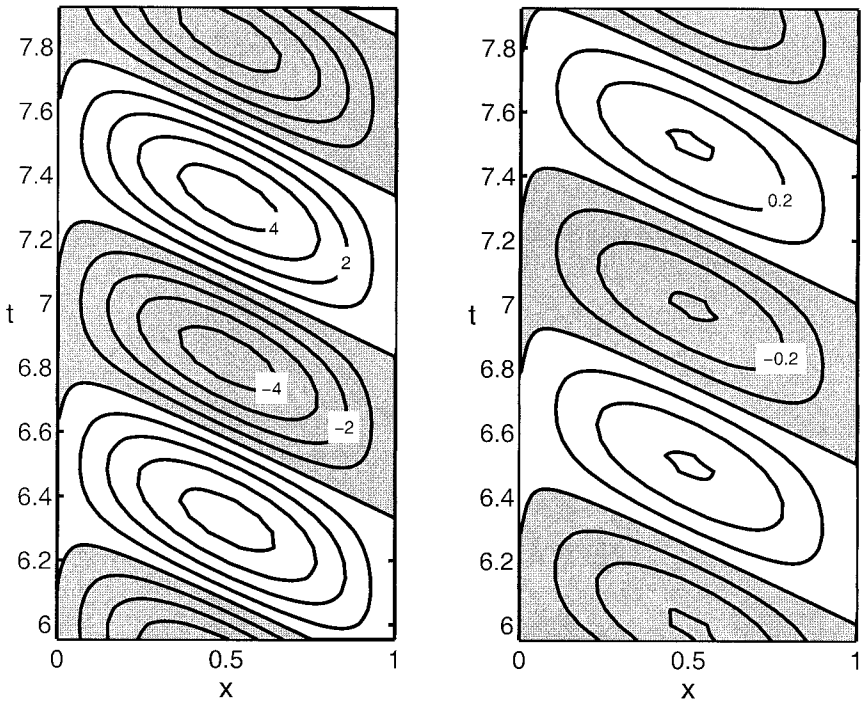

FIG. 12. Two time–longitude plots of the dynamical streamfunction, at $y = 0.5$, solution of (3.8), for $G = \sin 2\pi t$, and the other parameters are as in Fig. 8 except that $\delta = 3 \times 10^{-3}$: (left) the solution for the mass conserving boundary condition (2.2); (right) the incorrect boundary condition (2.3). The contour interval is 1.0 in the left panel and 0.1 in the right panel, and negative values are shaded.

ing Rossby wave transit times, indicate that the least damped modes have decadal frequencies. This suggests that the decadal low frequency described here survives the generalization to a fully hemispherical, shallow water description.

It is likely that on such long timescales, the redistribution of heat in the upper ocean associated with these large-scale oscillations affects the atmospheric circulation, and there is evidence from atmospheric general circulation models of a low-frequency atmospheric response elicited by oceanic heat content anomalies (Rodwell et al. 1999). Therefore, even if the observed response of the ocean appears in concert with the atmospheric forcing, as suggested by Sturges and Hong (1995), one cannot exclude that these low-frequency atmospheric fluctuations are actually driven by the oceanic dynamics.

Acknowledgments. Numerous conversations with Glenn Flierl, Myrl Hendershott, Joe Pedlosky, and Bill Young are gratefully acknowledged. Funding for this research is provided by the National Science Foundation and the Department of Energy.

REFERENCES

Anderson, D. L. T., and A. E. Gill, 1975: Spin-up of a stratified ocean, with applications to upwelling. *Deep-Sea Res.,* **22,** 583–596.

Cane, M. A., and E. S. Sarachik, 1977: Forced baroclinic ocean motions. II: The linear equatorial bounded case. *J. Mar. Res.,* **35,** 395–432.

——, and D. W. Moore, 1981: A note on low-frequency equatorial basin modes. *J. Phys. Oceanogr.,* **11,** 1578–1584.

Cox, M. D., 1987: An eddy-resolving numerical model of the ventilated thermocline: Time dependence. *J. Phys. Oceanogr.,* **17,** 1044–1056.

Flierl, G. R., 1977: Simple applications of McWilliams ''A note on a consistent quasi-geostrophic model in a multiply connected domain.'' *Dyn. Atmos. Oceans.,* **1,** 443–453.

Larichev, V. D., 1974: Statement of an internal boundary-value problem for the Rossby wave equation. *Izv. Atmos. Oceanic Phys.,* **10,** 470–473.

McWilliams, J. C., 1977: A note on a consistent quasigeostrophic model in a multiply connected domain. *Dyn. Atmos. Oceans,* **1,** 427–441.

Milliff, R. F., and J. C. McWilliams, 1994: The evolution of boundary pressure in ocean basins. *J. Phys. Oceanogr.,* **24,** 1317–1338.

Pedlosky, J., 1987: *Geophysical Fluid Dynamics.* Springer-Verlag, 710 + xiv pp.

Rhines, P. B., and W. R. Young, 1982: Homogenization of potential vorticity in planetary gyres. *J. Fluid Mech.,* **122,** 347–367.

Rodwell, M. J., D. P. Rowell, and C. K. Folland, 1999: Oceanic forcing of the wintertime North Atlantic Oscillation and European climate. *Nature,* **398,** 320–323.

Sturges, W., and B. G. Hong, 1995: Wind forcing of the Atlantic thermocline along 32°N at low frequencies. *J. Phys. Oceanogr.,* **25,** 1706–1715.

——, ——, and A. J. Clarke, 1998: Decadal wind forcing on the North Atlantic subtropical gyre. *J. Phys. Oceanogr.,* **28,** 659–668.